



Cite this: *Sustainable Energy Fuels*,  
2025, 9, 3404

# Graphene oxide conformally wrapped FeOOH/graphite composite anodes for lithium-ion batteries†

Periyasamy Anushkaran,<sup>a</sup> Yu Lim Lee,<sup>b</sup> Seong Hui Kim,<sup>a</sup> Su Hyeon Ahn,<sup>ac</sup>  
Du Hyun Lim,<sup>\*ac</sup> Hyun Gyu Kim<sup>\*d</sup> and Jum Suk Jang<sup>id \*ab</sup>

$\beta$ -FeOOH is among the most prevalent anode materials used in lithium-ion batteries (LIBs) due to its high theoretical specific capacity. However, the practical use of such anodes is severely constrained by their limited electrical conductivity and mechanical damage resulting from volume changes during electrochemical cycling. Herein, to circumvent these issues, an environmentally benign synthesis of FeOOH nanorods on graphite sheets encapsulated in a graphene oxide (GO) layer was designed. Graphite mitigated the agglomeration of FeOOH nanorods and provided a conductive network. In addition, GO alleviated volume expansion and established a denser solid-electrolyte interface during the initial cycle, which prevents excessive consumption of Li-ions and maintains cycle life and capacity. The resultant GO@Gr-FeOOH anode demonstrated outstanding electrochemical properties, with an extended lifespan and superior Li-ion diffusion coefficient. Accordingly, the GO@Gr-FeOOH sample retained a capacity of 716 mAh g<sup>-1</sup> at 0.2 C after 50 cycles and 428.7 mAh g<sup>-1</sup> at 0.5 C after 150 cycles. Therefore, this study presents an effective and practical approach to address the constraints of FeOOH-based anode materials using hybridization with diverse carbon component strategies.

Received 11th February 2025  
Accepted 2nd May 2025

DOI: 10.1039/d5se00202h  
rsc.li/sustainable-energy

## Introduction

Lithium-ion batteries (LIBs) are widely recognized as promising energy storage devices in the sectors of electric vehicles and portable electronic devices due to their high operation voltage, minimal self-discharge, high energy density and eco-friendliness.<sup>1–3</sup> In recent years, new electrode materials have been studied to satisfy the increasing demand for higher capacity.<sup>4,5</sup> Transition metal oxides are regarded as potential contenders for high-performance LIB anodes based on their high theoretical capacity (700–1000 mA h g<sup>-1</sup>).<sup>6</sup> One of the materials,  $\beta$ -FeOOH (FeOOH), has the qualities of cost-effectiveness, non-toxicity and high theoretical capacity (905 mAh g<sup>-1</sup>).<sup>7,8</sup> Ever since Amine and his colleagues reported the use of tunnel-structured FeOOH in LIBs in 1999,<sup>9</sup> numerous studies have explored its potential as a high-performance anode

for LIBs.<sup>10–12</sup> Nevertheless, poor electrical conductivity, sluggish reaction kinetics and the volume fluctuation of FeOOH throughout the lithiation/delithiation processes result in the unavoidable deterioration of its structure and consequently, low capacity retention. The combination of structural collapse and the low conductivity of FeOOH leads to a significant decrease in capacity over extended cycles.<sup>13,14</sup>

Several modification strategies have been devised to achieve high-performance anodes based on FeOOH. Nanostructuring has been an extensively esteemed approach to enhance the electrochemical performance of FeOOH.<sup>15,16</sup> The Li<sup>+</sup> transport distance can be shortened and the volume variation can be reduced through the use of nanostructure design, resulting in FeOOH electrodes with enhanced Li storage performance.<sup>10</sup> Compositing with conductive carbon-based materials is the main approach to enhance the lithium storage performance.<sup>17–19</sup> The hybridization of nanostructured FeOOH with carbon components is another effective method that can be utilized to resolve concerns such as inadequate cycle life and rate capability.<sup>7,20</sup> Such carbon materials can provide networks that are both flexible and conductive and effectively inhibit the aggregation of particles and boost the electrical conductivity of FeOOH. Consequently, FeOOH-carbon hybrids demonstrate a significant improvement in cycling and rate capabilities.<sup>14</sup>

To date, several types of carbon materials have been coated with an FeOOH anode for use in LIBs. By synthesizing FeOOH on functionalized porous carbon, Zhu and co-workers achieved

<sup>a</sup>Department of Integrative Environmental Biotechnology, College of Environmental and Bioresource Sciences, Jeonbuk National University, Iksan 54596, Republic of Korea. E-mail: jangjs75@jbnu.ac.kr

<sup>b</sup>Division of Biotechnology, College of Environmental and Bioresource Sciences, Jeonbuk National University, Iksan 54596, Republic of Korea

<sup>c</sup>Energy 11. Co. Ltd, 122 Bongdong-eup, Wanjusandan 9-ro, Wanju-Gun, Jeollabuk-do, 55315, Republic of Korea. E-mail: duhyun@energy11.co.kr

<sup>d</sup>Busan Center, Korea Basic Science Institute (KBSI), Busan 46742, Republic of Korea. E-mail: hhgkim@kbsi.re.kr

† Electronic supplementary information (ESI) available. See DOI: <https://doi.org/10.1039/d5se00202h>

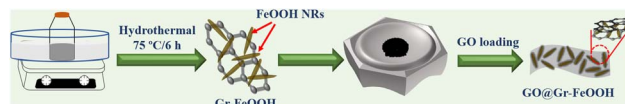
a reversible capacity of 446.1 mAh g<sup>-1</sup> at 1 A g<sup>-1</sup> after 1000 cycles.<sup>20</sup> In addition, pine-biomass carbon-adhered FeOOH nanorods (NRs) retained a specific capacity of 660 mAh g<sup>-1</sup> at 0.2 C after 450 cycles.<sup>21</sup> Graphite, in particular, is widely utilized as an additive for LIB anodes as it possesses good electrical conductivity and mechanical potential. For example, Beletskii *et al.* fabricated an atmospheric plasma-assisted FeOOH/graphite composite.<sup>22</sup> However, to the best of our knowledge, no research has been performed on FeOOH NRs grown on graphite by hydrothermal synthesis. The inclusion of only graphite could not enhance the charge conductivity of pure FeOOH to facilitate its high rate operating efficiency in LIBs.

The aforementioned issue may be resolved through the use of a graphene-based matrix system, as several studies have demonstrated that active-material/graphene composites can significantly improve the charge conductivity and ion diffusion of Li ions in electrodes.<sup>23,24</sup> Likewise, FeOOH derives advantages from composite systems employing materials based on graphene oxide (GO). For instance, microwave-treated GO-FeOOH retained a specific capacity of 304 mAh g<sup>-1</sup> after undergoing 1000 cycles at 5 A g<sup>-1</sup>.<sup>25</sup> Moreover, Chen *et al.* reported that the FeOOH/GO anode retained 93.35% of its initial stability after 100 cycles at 1 A g<sup>-1</sup>.<sup>16</sup> These findings demonstrate the potential of GO to enhance both conductivity and stability. With the knowledge gained from these studies, we believe that the incorporation of nanostructuring, graphite and GO hybridization could significantly augment the Li storage and Li<sup>+</sup> diffusion kinetics of FeOOH-based anodes.

Accordingly, the purpose of this research was to develop a novel GO-encapsulated FeOOH/graphite anode material for use in an LIB. FeOOH NRs were affixed to graphite sheets using a simple hydrothermal approach. GO was subsequently ground with an FeOOH/graphite material to affect the kinetics of electrochemical reactions and structural regulation. The rationally constructed GO@Gr-FeOOH anode ensured conductive channels and effectively mitigated the volume expansion of FeOOH. In comparison to bare FeOOH (206.7 mAh g<sup>-1</sup>), the GO@Gr-FeOOH composite delivered an enhanced cyclability, retaining a capacity of 428.7 mAh g<sup>-1</sup> at 0.5 C after 150 cycles.

## Experimental

2.0 g of graphite powder (60 wt%) (purchased from POSCO; particle size of 16 μm) was dispersed in deionized water (DIW) by ultrasonication for 30 min prior to adding precursors. A solution of 150 mM FeCl<sub>3</sub>·6H<sub>2</sub>O and 1 M NaNO<sub>3</sub> in 100 mL deionized water (DIW) was added, and the mixture was adjusted to a pH of 1.5. The aforementioned mixture was transferred to an oil bath for hydrothermal treatment, with continuous agitation at 75 °C for 6 h, after 10 mL of ethanol was added. Once cooled to room temperature, the precursor was filtered, rinsed several times with DIW and dried overnight at 80 °C to obtain 60%Gr-FeOOH. The GO coating was achieved by mixing 0.70 g Gr-FeOOH and 0.125 g GO (purchased from Graphene Supermarket; single-layer GO; particle size of ~0.7 μm) and grinding in ethanol. The sample obtained is referred to as



Scheme 1 Schematic representation for the fabrication of GO@Gr-FeOOH.

GO@Gr-FeOOH. Scheme 1 represents the fabrication process of the GO@Gr-FeOOH sample.

## Results and discussion

The optimized parameters of graphite modification and GO loading are depicted in Fig. S1 and S2,<sup>†</sup> respectively. The structural features of the materials were examined using X-ray diffraction (XRD), as depicted in Fig. 1a, proving the presence of β-FeOOH with the corresponding diffraction peaks (JCPDS No. 34-1266).<sup>26</sup> In addition, the peak intensity at 26.5° increased for the Gr-FeOOH and GO@Gr-FeOOH samples compared to bare FeOOH because the graphite peak at the (002) plane is more prominent.<sup>24</sup> The existence of two peaks at 44.4 and 54.6°, belonging to (101) and (004) planes, respectively (JCPDS No. 41-1487), substantiated the graphitic nature of the samples.<sup>27</sup> Fig. S3<sup>†</sup> depicts the XRD pattern of graphite. The elemental composition and valence state of the as-prepared anode materials were investigated using XPS. The XPS spectra of Fe 2p exhibited two prominent peaks, accompanied by two shake-up satellite peaks (sat.) at 711.6 (Fe 2p<sub>3/2</sub>), 725.2 (Fe 2p<sub>1/2</sub>), 719.2 (Fe 2p<sub>3/2</sub> sat.) and 733.3 eV (Fe 2p<sub>1/2</sub> sat.) (Fig. S4<sup>†</sup>), representing the +3 chemical state of Fe in the synthesized FeOOH.<sup>28</sup> Moreover, Fe 2p XPS spectra revealed satellite peaks at 719.2 and 733.3 eV, indicative of Fe<sup>3+</sup>. Besides, there are no observable satellite peaks at around 716 and 730 eV, confirming the absence of Fe<sup>2+</sup>. Additionally, the Fe 2p<sub>3/2</sub> satellite peak is positioned almost 8 eV higher than the foremost peak, which also further attests to the Fe<sup>3+</sup>.<sup>29–31</sup> As shown in Fig. 1b, the O 1s spectra contained peaks at 530.3, 531.5, 532 and 532.9 eV, which were assigned to lattice oxygen (Fe–O), surface-adsorbed OH<sup>-</sup>, C–O, and surface-adsorbed water, respectively.<sup>32,33</sup>

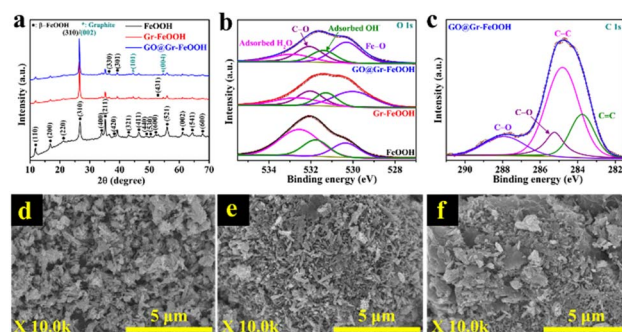


Fig. 1 (a) XRD patterns, (b) XPS spectra of O 1s for FeOOH, Gr-FeOOH and GO@Gr-FeOOH samples, (c) XPS spectra of C 1s for the GO@Gr-FeOOH sample; HR FE-SEM top view images of (d) FeOOH, (e) Gr-FeOOH and (f) GO@Gr-FeOOH samples.

Deconvolution of the C 1s spectra for the GO@Gr-FeOOH sample was executed using four Gaussian curves (Fig. 1c), representing C=C (283.8 eV), C-C (284.8 eV), C-O (285.3 eV), and C=O (287.9 eV).<sup>34,35</sup>

The morphological features of FeOOH, Gr-FeOOH and GO@Gr-FeOOH were assessed by FE-SEM (Fig. 1d–f and S5†), and all samples exhibited a rod-like structure. The bare-FeOOH NRs were agglomerated (Fig. S5a†), while the presence of graphite inhibited such agglomeration and maintained greater surface area (Fig. S5b†). Furthermore, as can be seen from Fig. 1f, S5c and f,† GO coated the surfaces of the NRs and facilitated interconnections among the FeOOH NRs. Fig. S6† shows the morphology of graphite. The compositional studies of the anode materials have been done based on the SEM-EDS (Fig. S7–S9 and Table S1†) and semi-quantitative analysis (SQX), which is an application of wavelength-dispersive X-ray fluorescence (XRF) spectrometry (Table S2†). The SQX analysis revealed an O/Fe atomic ratio of approximately 1.38, which is significantly lower than the stoichiometric ratio expected for FeOOH (2.0). Combined with the observation of an intense background in the XRD pattern, these results suggest that the majority of the samples consist of an X-ray-amorphous, oxygen-deficient oxyhydroxide phase. Therefore, it is speculated that the synthesized material primarily comprises a highly disordered, low-oxygen iron-based phase, rather than pure, crystalline FeOOH.

Fig. 2a displays the Fourier transform infrared (FT-IR) spectra of FeOOH, Gr-FeOOH and GO@Gr-FeOOH. The broad peaks at  $\sim 3360$  and  $1615\text{ cm}^{-1}$  arose from the stretching and bending vibrations of O–H, respectively, in FeOOH.<sup>36</sup> The detected FT-IR absorption bands in the range of 670 and  $\sim 850\text{ cm}^{-1}$  were attributed to Fe–O symmetric stretching and O–H bending vibrations, respectively.<sup>37,38</sup> The band observed at  $1580\text{ cm}^{-1}$  belongs to the C=C ( $\text{sp}^2$  carbon). Specifically, the peak intensity at  $1580\text{ cm}^{-1}$  increased for GO@Gr-FeOOH,

explicitly indicating the GO modification. Furthermore, it was shown that the distinctive peaks for GO at  $1720$  and  $2850\text{--}2920\text{ cm}^{-1}$  were related to the stretching vibrations of C=O and C–H, respectively.<sup>7,39,40</sup> Transmission electron microscopy (TEM) images were acquired to identify the microstructure of GO@Gr-FeOOH. As shown in Fig. 2b, GO@Gr-FeOOH exhibited a rod-like shape. The indicated lattice fringe with a  $d$ -spacing of  $0.259\text{ nm}$  belongs to the (400) lattice plane of FeOOH (Fig. 2c), which is consistent with the above XRD data. Moreover, it is evident that the FeOOH rods were conformally coated with GO with a thickness of  $\sim 15\text{ nm}$  (Fig. 2d). The corresponding elemental mapping and spectral analysis verified the presence of Fe, O and C (Fig. 2e and S10†). Furthermore, as can be seen from Fig. 2f and S11,† the EDS line scanning revealed the homogeneous distribution of Fe and O throughout the NR. Also, carbon is conspicuously observed on the exterior of the NR, validating the GO encapsulation on the surface of the FeOOH (Fig. S12†).

Cyclic voltammetry (CV) tests were conducted at a scan rate of  $0.1\text{ mV s}^{-1}$  to examine the lithiation/delithiation behavior, with comparative data provided in Fig. 3a–c. The initial discharge curve has three peaks at 1.59, 1.05 and 0.64 V. The cathodic peaks at 1.59 and 1.05 V are associated with the insertion of  $\text{Li}^+$  into FeOOH to generate  $\text{Li}_x\text{FeOOH}$ , and the phase transformation and structural changes of FeOOH during  $\text{Li}^+$  intercalation, respectively.<sup>8,38</sup> Furthermore, the noticeable cathodic peak at 0.64 V is linked to the formation of the solid-electrolyte interface (SEI) as well as the conversion reaction resulting in metallic  $\text{Fe}^0$ .<sup>16,20</sup> During the subsequent first anodic scan, a distinct peak at 1.07 V was assigned to the deformation of the SEI and a broad peak at 1.5–1.75 V is ascribed to the deconversion reaction of  $\text{Fe}^0$  to  $\text{Fe}^{3+}$ .<sup>41,42</sup> As the number of cycles increases, the peak currents significantly diminish, leading to irreversible capacity loss due to the unstable characteristics of the FeOOH electrode.<sup>7</sup> After the second cycle, however, the peak currents begin to overlap. This phenomenon can be related to the influence that graphite and GO have on the stabilization of the SEI layers (Fig. 3b and c). Also, the SEI deformation peak almost disappeared after the fifth cycle for graphite-modified samples, substantiating the establishment of a stable SEI.<sup>43</sup> Moreover, noticeable cathodic and anodic peaks were observed at 0.17 and 0.24 V for Gr-FeOOH and GO@Gr-FeOOH anodes. These peaks are responsible for the intercalation of  $\text{Li}^+$  into graphite and the deintercalation of  $\text{Li}^+$  from graphite, respectively.<sup>44</sup>

Galvanostatic cycling experiments of the synthesized FeOOH, Gr-FeOOH and GO@Gr-FeOOH anodes were conducted at 0.1 C, as depicted in Fig. 3d, with the initial five cycles presented in Fig. S13.† The discharge/charge capacities of FeOOH, Gr-FeOOH and GO@Gr-FeOOH in the first cycle were 1390/1140, 790/643 and 1183/850  $\text{mA h g}^{-1}$ , with initial coulombic efficiencies (ICEs) of 82.2, 81.7 and 71.7%, respectively. Two plateaus are noted during the first discharge at  $\sim 1.85\text{ V}$ , indicating  $\text{Li}^+$  intercalation to generate  $\text{Li}_x\text{FeOOH}$  and at  $\sim 0.8\text{ V}$ , attributed to the SEI formation and the conversion reaction yielding  $\text{Fe}^0$ . The ICE of GO@Gr-FeOOH was inferior to that of the other two anodes. This could be ascribed to the

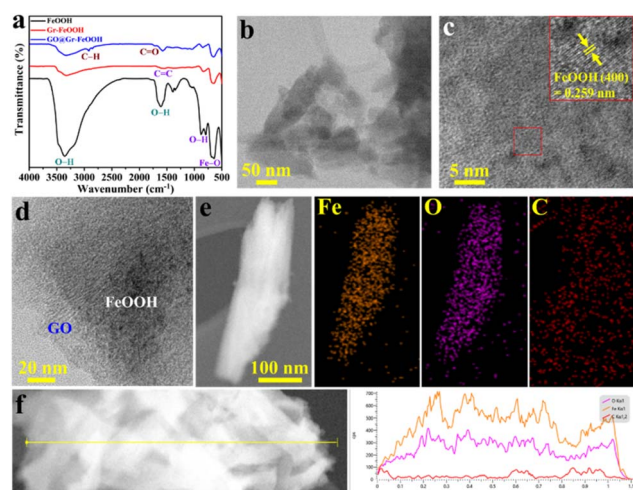


Fig. 2 (a) FT-IR spectra of FeOOH, Gr-FeOOH and GO@Gr-FeOOH samples; and (b) TEM, (c and d) HR-TEM images, (e) EDS elemental mapping images and (f) EDS line scanning of the GO@Gr-FeOOH sample.



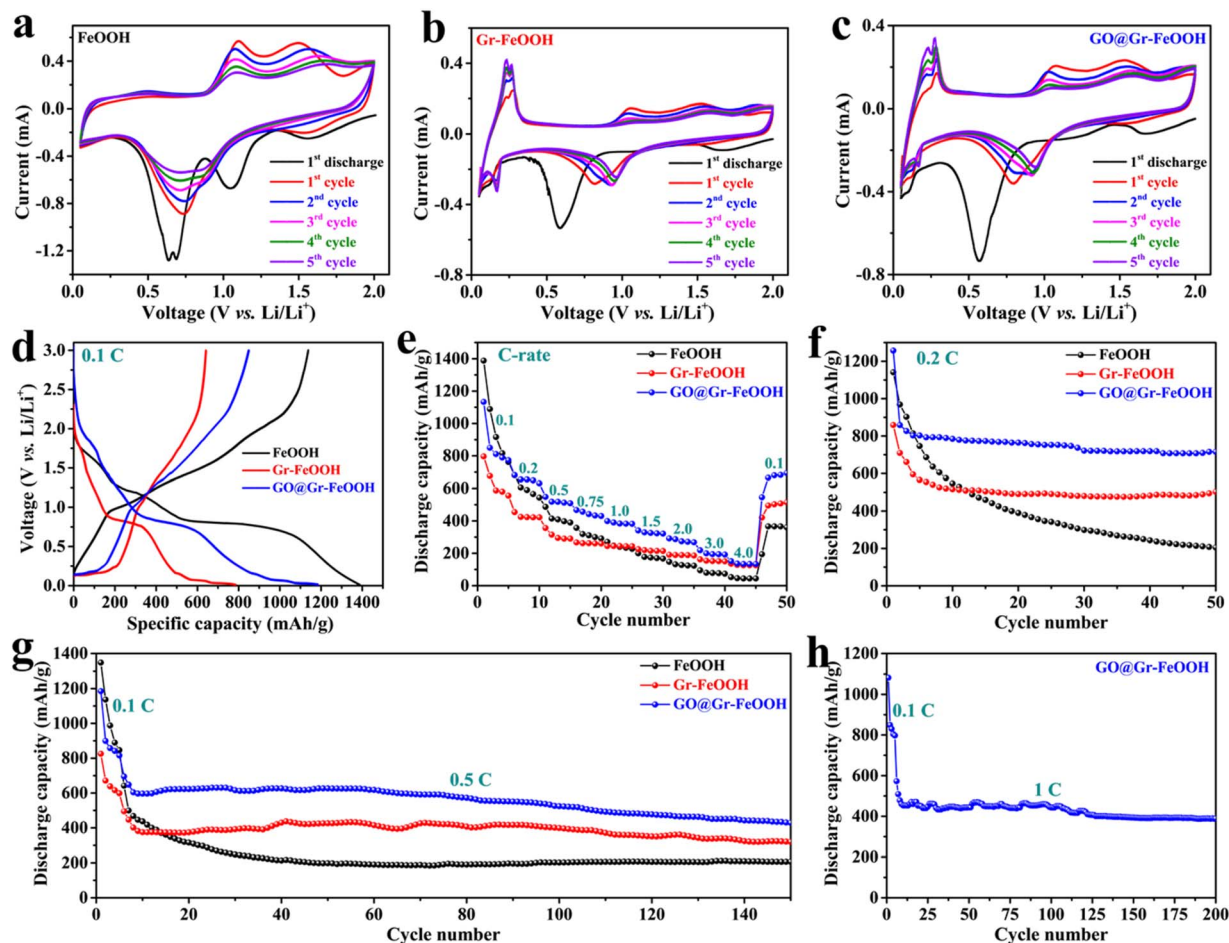


Fig. 3 CV curves at a scan rate of 0.1 mV s<sup>-1</sup> of (a) FeOOH, (b) Gr-FeOOH and (c) GO@Gr-FeOOH; (d) initial discharge–charge profiles at 0.1 C, (e) rate performance from 0.1 to 4.0 C, (f) cycle performance at 0.2 C, (g) long-cycle stability test at 0.5 C (after activation at 0.1 C for 5 cycles) of FeOOH, Gr-FeOOH and GO@Gr-FeOOH samples; and (h) long-cycle stability test at 1 C (after activation at 0.1 C for 5 cycles) of the GO@Gr-FeOOH anode.

development of a denser organic SEI, leading to a marginally reduced ICE. This thicker SEI layer formed in the GO@Gr-FeOOH may result from the incorporation of GO, which offers an expanded contact area with the electrolyte. It is noteworthy that the initial discharge capacities of both FeOOH and GO@Gr-FeOOH are higher than the theoretical capacity of FeOOH. This might be due to the irreversible and partially irreversible reactions that transpired during the initial discharge process as a result of the formation of the SEI. The formation of the SEI may elicit reactions that enable further lithium storage. Besides, the electrolyte may decompose during cycling to generate the SEI, leading to the formation of additional lithium-containing species that can contribute to charge storage. Furthermore, transition metal oxides or carbon-based materials can store lithium through surface or near-surface reactions, which can result in additional capacity (pseudocapacitive).<sup>28,45,46</sup> In contrast, Gr-FeOOH exhibited a lower initial discharge capacity, which arose from graphite.

Cells with different C-rates were assessed to determine their rate capability and the results are depicted in Fig. 3e. Despite the fact that Gr-FeOOH showed lower capacities at low C-rates,

the discharge capacity rapidly recuperates to 510 mAh g<sup>-1</sup> when the current density reverts to 0.1 C. It should be noted, on the other hand, that bare FeOOH was only able to keep 48.6% of its discharge capacity after the rate cycles were completed. This result indicates that graphite has the potential to enhance the stability of FeOOH. The GO-modified Gr-FeOOH demonstrated superior capacity across all current rates. It is noteworthy that, even at a high current density of 2 C, the GO@Gr-FeOOH electrode retained 35% of the initial reversible capacity at 0.1 C. This outcome indicates that the GO@Gr-FeOOH anode exhibited exceptional kinetics. We presume that this is a consequence of the inclusion of GO around and interlinking individual FeOOH NRs, which increased the electrical conductivity of the electrode. Additionally, we tested the cycling stability at a rate of 0.2 C. As can be observed in Fig. 3f, the FeOOH, Gr-FeOOH and GO@Gr-FeOOH samples retained 21.2, 70.9 and 83.5% capacity, respectively, after the 50<sup>th</sup> cycle relative to the 2<sup>nd</sup> cycle. The cycling performance of the as-prepared anodes at 0.5 C is illustrated in Fig. 3g. Following activation at 0.1 C for five cycles, GO@Gr-FeOOH demonstrated a reversible specific capacity of 428.7 mAh g<sup>-1</sup>, with a capacity retention of 61.7% at

0.5 C after 150 cycles, accompanied by an average CE of 98% (Fig. S14†). Conversely, FeOOH and Gr-FeOOH displayed reversible specific capacity values of 206.7 and 319.7 mAh g<sup>-1</sup>, respectively, with capacity retentions of 32.2 and 60.5% at 0.5 C after 150 cycles. The low capacity of FeOOH is attributable to its low conductivity and poor structural stability. The continuous volume fluctuations during lithiation and delithiation caused structural instability in FeOOH, resulting in pulverization and rapid capacity loss. The improved capacity and stability of the graphite/FeOOH composite can be attributed to the conductive graphite network that aids electron transmission, while simultaneously preventing FeOOH aggregation, offering increased active sites for Li-ion storage. The well-designed GO-coated structure was the reason for the exceptional cycling performance of GO@Gr-FeOOH, where the GO@Gr-FeOOH anode showed 388.6 mAh g<sup>-1</sup> of reversible specific capacity after 200 cycles at 1 C (Fig. 3h), with a capacity retention of 67.8% (from the 6<sup>th</sup> cycle). The GO modification resulted in a thicker SEI during the initial cycle (as we discussed earlier). This thick SEI layer can effectively passivate the surface of the anode and prevent further electrolyte decomposition. It led to minimizing Li-ion consumption, ultimately improving cycling stability.

Electrochemical impedance spectroscopy (EIS) measurements were conducted before cycling to gain a more comprehensive understanding of the electrochemical reaction of the as-fabricated anode samples. Nyquist plots were simulated based on the equivalent circuit model (inset of Fig. 4a) to derive the parameters associated with electrolyte resistance ( $R_s$ ), charge transfer resistance at the electrode/electrolyte interface ( $R_{ct}$ ) and Warburg impedance ( $Z_w$ ). Fig. 4a illustrates that Gr-FeOOH somewhat reduced  $R_{ct}$  from 293.6 to 270.4  $\Omega$  before cycling. Furthermore,  $R_{ct}$  dramatically decreased for the GO@Gr-FeOOH anode (91  $\Omega$ ), implying that the GO wrapping facilitated an acceleration of the charge transfer rate between the electrode and electrolyte, which is advantageous for the

reduction of  $R_{ct}$ . This can be attributed to the GO coating, which can buffer volume changes of FeOOH, thereby retaining the structural integrity and preventing the disruption of conductive pathways. In addition, the functional groups of GO can interact with Li-ions and facilitate their transport at the interface.<sup>47</sup> Additionally, in order to evaluate the effect of GO coating amount on the charge transfer behaviour, we analyzed the EIS and depicted it in Fig. S15.† As shown in Table S3,† the 0.125-GO@Gr-FeOOH sample showed the lowest  $R_{ct}$ , implying the improved Li-ion insertion/transport. Moreover, we estimated the Li<sup>+</sup> diffusion coefficient ( $D_{Li^+}$ ) prior to cycling through EIS analysis utilizing the subsequent equation:<sup>48</sup>

$$D_{Li^+} = 0.5 \left( \frac{RT}{AF^2 n^2 C \sigma_w} \right)^2 \quad (1)$$

$$Z'_{Re} = R_s + R_{ct} + \sigma_w \omega^{-0.5} \quad (2)$$

where,  $R$  is the universal gas constant (8.314 J mol<sup>-1</sup> K<sup>-1</sup>),  $T$  is the absolute temperature,  $A$  is the surface area of the electrode,  $F$  is the Faraday constant (96485 C mol<sup>-1</sup>),  $n$  is the number of electrons transferred per reaction (1 per 1 Li-ion),  $C$  is the Li-ion bulk concentration in the electrolyte (0.001 mol cm<sup>-3</sup>) and  $\sigma_w$  is the Warburg factor determined by  $Z'_{Re}$  and  $\omega^{-0.5}$ . Fig. 4b displays the linear correlation between  $Z'_{Re}$  and  $\omega^{-0.5}$  and Gr-FeOOH had a 1.5-times increase in  $D_{Li^+}$  relative to bare-FeOOH (Fig. S16†). Additionally, GO@Gr-FeOOH exhibited a 20-fold improvement in  $D_{Li^+}$  compared to Gr-FeOOH. The enhancement of the ion diffusion coefficient may result from the oxygen-containing functional groups of GO created spacing that provided channels for Li-ion transport. Additionally, GO possessed a large surface area, augmenting the effective surface area of the FeOOH, thereby increased the number of active sites for Li-ion intercalation. Furthermore, by reducing the  $R_{ct}$ , GO contributed to a reduction in the electrochemical polarization of the FeOOH electrode.<sup>49,50</sup>

In order to estimate the impact of the SEI layer, we performed the EIS analysis of the FeOOH, Gr-FeOOH and GO@Gr-FeOOH samples following the 150-cycle stability test. As shown in Fig. S17,† the Nyquist plots were fitted according to the equivalent circuit model (inset of Fig. S17†).  $R_{SEI}$  is the resistance originating from the SEI. The fitted parameters are provided in Table S4.† As can be seen from Fig. S17,† it is obvious that the GO@Gr-FeOOH had the smallest semicircle, signifying that its resistances are significantly lower than those of other samples. It is evident that the  $R_s$  of FeOOH and Gr-FeOOH anodes exhibited higher values. This rise in resistance is primarily attributed to the accumulation of electrolyte decomposition by-products and the thickening of the SEI layer. The FeOOH anode, renowned for its high redox activity, can facilitate parasitic side reactions, specifically under prolonged cycling conditions, leading to the formation of resistive organic and inorganic species such as LiF and RCO<sub>2</sub>Li. It is possible that, with time, electrolyte depletion and increased viscosity resulting from solvent breakdown may also impede efficient lithium-ion transport, which would further elevate the electrolyte resistance.<sup>51–53</sup> Besides, the bare FeOOH sample showed an

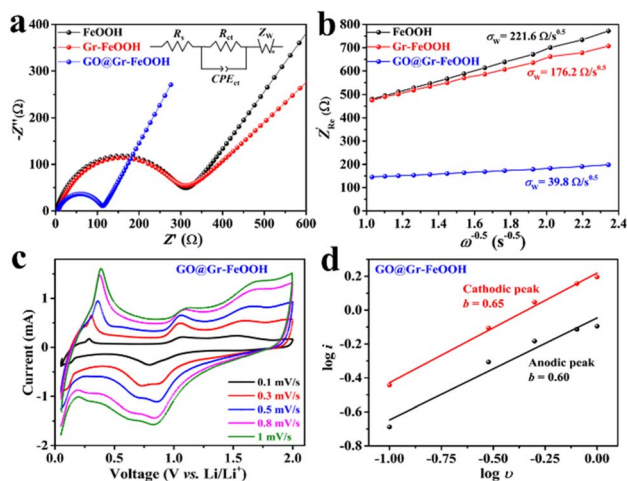


Fig. 4 (a) EIS spectra before cycling (inset: corresponding equivalent circuit), (b) relation curve between  $Z'_{Re}$  and  $\omega^{-0.5}$  at low frequencies of FeOOH, Gr-FeOOH and GO@Gr-FeOOH; (c) CV curves of GO@Gr-FeOOH at different scan rates and (d) relation curve between  $\log i$  and  $\log \nu$  of the GO@Gr-FeOOH anode.

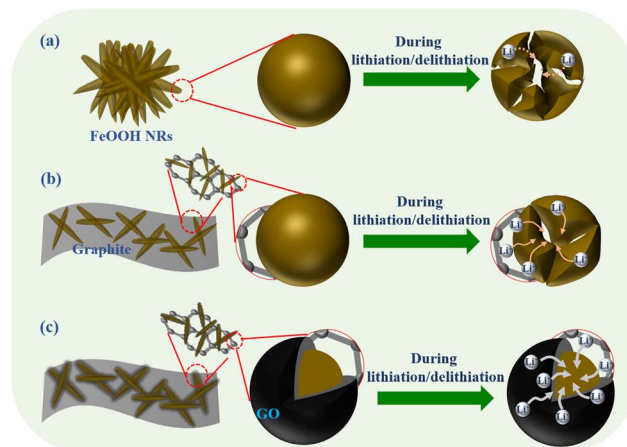
increase in  $R_{\text{SEI}}$  as a result of the thick SEI, which impaired the ion transfer. Moreover, it is apparent that the GO coating diminished the  $R_{\text{SEI}}$  and  $R_{\text{ct}}$ . The GO coating played a crucial role in suppressing SEI growth and stabilizing the electrode/electrolyte interface, causing a notable decrease in both  $R_{\text{SEI}}$  and  $R_{\text{ct}}$  after long-term cycling compared to bare FeOOH. GO formed an electrically conductive and chemically stable interfacial layer on the FeOOH surface. This layer served as a physical barrier, preventing direct contact between FeOOH and the electrolyte, thereby minimizing parasitic reactions and inhibiting continuous SEI formation. Additionally, the functional groups of GO contributed to uniform and thinner SEI formation.<sup>16,25</sup>

In order to explore the capacitive features of the GO@Gr-FeOOH anode, the CVs at various scan rates were obtained, as seen in Fig. 4c. The  $\text{Li}^+$  storage mechanism can be classified into two components: the faradaic contribution arising from the diffusion of  $\text{Li}^+$  into the bulk of the material, which governs the redox reaction as a battery process and the capacitive behavior, which consists of the faradaic contribution from the charge-transfer process at the surface, known as pseudocapacitance, or the non-faradaic contribution from the double-layer capacitive effect.<sup>54</sup> The following equation can be used to assess the impact of capacitive behavior by plotting peak current ( $i$ ) against the scan rate ( $\nu$ ):<sup>55</sup>

$$i = a\nu^b \quad (3)$$

The parameters  $a$  and  $b$  both are adjustable. The  $b$  value denotes the different kinetic processes of the electrochemical reaction ( $\text{Li}^+$  storage mechanism of material): when the  $b$  value is near 0.5, it signifies that charge transfer is primarily governed by a diffusion-controlled process, whereas a  $b$  value approaching 1 indicates that the system is predominantly controlled by the capacitance process.<sup>56</sup> As can be seen from Fig. 4d, the values of  $b$  for the anodic and cathodic peaks are 0.60 and 0.65, respectively. The fact that this result was obtained indicates that the  $\text{Li}^+$  storage mechanism in the GO@Gr-FeOOH anode is a combination of processes that are controlled by diffusion and capacitive regulation.

Based on our investigations, we suggested a plausible mechanism for bare FeOOH, Gr-FeOOH and GO@Gr-FeOOH anodes during lithiation/delithiation processes (Scheme 2). The FeOOH anode experienced continuous volume expansion and contraction during the Li-ion intercalation and deintercalation (as explained by CV), which led to formation of cracks, particle pulverization, and serious capacity fading (Scheme 2a). The  $\text{sp}^2$ -bonded carbon layers of graphite can create a conductive matrix for FeOOH NRs. This markedly enhanced the electron transport, improving the overall charge/discharge kinetics of the anode (Scheme 2b). Besides, graphite facilitated the dispersion of FeOOH particles and inhibited their agglomeration. Through the consistent distribution of FeOOH with the graphite matrix, a high active surface area was maintained, which resulted in an increase in the number of Li-ion storage sites and a more favourable interaction with the electrolyte, ultimately leading to an increase in total capacity. In



Scheme 2 Schematic illustrations for the lithiation/delithiation mechanism of (a) FeOOH, (b) Gr-FeOOH and (c) GO@Gr-FeOOH samples.

the case of the GO@Gr-FeOOH anode (Scheme 2c), GO functioned as a mechanical support for FeOOH NRs, thereby suppressing volume variations in the GO@Gr-FeOOH anode. This resulted in improved cycle stability and reduced material pulverization. Also, GO can promote the formation of a stable and uniform SEI layer on the FeOOH surface, protecting it from continuous degradation while allowing Li-ion transport. Moreover, the chemical interaction between FeOOH and GO consistently stabilized the FeOOH NRs and afforded a path for Li-ion transport.

## Conclusions

In summary, GO-encapsulated FeOOH/graphite was successfully fabricated to address the intrinsic drawbacks of FeOOH electrodes, including low electrical conductivity and volumetric expansion during cycling. The GO@Gr-FeOOH anode showed a remarkable capacity of  $680 \text{ mAh g}^{-1}$  at 0.1 C, despite cycling at numerous current rates. This capacity is 90 and 33% better than those of bare FeOOH and Gr-FeOOH, respectively. Furthermore, a discharge capacity of  $388.6 \text{ mAh g}^{-1}$  was sustained by the GO@Gr-FeOOH electrode even after 200 cycles at 1 C. The synergistic effect of the graphite sheet and GO wrapping was responsible for the high stability of the GO@Gr-FeOOH anode. Graphite acted as a conductive matrix to accelerate ion transmission. In addition, the conformally enveloped GO layer offered an increased number of active sites for Li-ion intercalation, while GO accommodated the volumetric fluctuations of FeOOH, ensuring structural integrity. The suggested approaches for the FeOOH anode in this study can be employed for other transition metal oxide-based anode materials to tackle identical issues and optimize their performance.

## Data availability

The data supporting this article have been included as part of the ESI.†



## Conflicts of interest

There are no conflicts to declare.

## Acknowledgements

This research was supported by the National Research Foundation of Korea (NRF) grant funded by the Korean government (MSIT) (NRF-2023R1A2C1003088).

## References

- 1 H. Fu, B. Gao, Y. Qiao, W. Zhu, Z. Liu, G. Wei, Z. Feng and A. R. Kamali, *Chem. Eng. J.*, 2023, **477**, 146936.
- 2 B. Zhu, D. Liu, L. Wang, B. Zhong and H. Liu, *J. Colloid Interface Sci.*, 2023, **643**, 437–446.
- 3 W. Wang, H. Tang, J. Cunha, M. Karimi, N. Lashari, A. Ahmad and H. Yin, *Energy Mater.*, 2025, **5**, 500008.
- 4 M. H. Hossain, M. A. Chowdhury, N. Hossain, M. A. Islam, M. and H. Mobarak, *Chem. Eng. J. Adv.*, 2023, **16**, 100569.
- 5 S. Yuan, Q. Lai, X. Duan and Q. Wang, *J. Energy Storage*, 2023, **61**, 106716.
- 6 J. Peng, N. Hu, A. Jin, M. Li, Z. J. Xu and L. Yu, *Next Mater.*, 2024, **3**, 100150.
- 7 H. Qi, L. Cao, J. Li, J. Huang, Z. Xu, Y. Cheng, X. Kong and K. Yanagisawa, *ACS Appl. Mater. Interfaces*, 2016, **8**, 35253–35263.
- 8 X. Liang, Z. Rong, B. Liang, Y. Xie, H. Huang, D. Huang, W. Zhou, S. Xu and J. Guo, *J. Mater. Sci.*, 2024, **59**, 3018–3030.
- 9 K. Amine, H. Yasuda and M. Yamachi, *J. Power Sources*, 1999, **81**, 221–223.
- 10 L. Yu, C. Wei, Q. Yan and Z. J. Xu, *Nano Energy*, 2015, **13**, 397–404.
- 11 W. Lianyang, L. Liqiang, Z. Chuangchuang, W. Xin and L. Xingyi, *Int. J. Electrochem. Sci.*, 2021, **16**, 210643.
- 12 L. He, C. Tan, C. Sheng, Y. Chen, F. Yu and Y. Chen, *Dalton Trans.*, 2020, **49**, 9268–9273.
- 13 B. Liang, S. Zhu, J. Wang, X. Liang, H. Huang, D. Huang, W. Zhou, S. Xu and J. Guo, *Appl. Surf. Sci.*, 2021, **550**, 149330.
- 14 S. Zhu, B. Liang, X. Mou, X. Liang, H. Huang, D. Huang, W. Zhou, S. Xu and J. Guo, *J. Alloys Compd.*, 2022, **905**, 164142.
- 15 Z. Zhao, H. Su, S. Li, C. Li, Z. Liu and D. Li, *J. Alloys Compd.*, 2020, **838**, 155394.
- 16 X. Chen, Y. Zeng, Z. Chen, S. Wang, C. Xin, L. Wang, C. Shi, L. Lu and C. Zhang, *Front. Chem.*, 2020, **8**, 328.
- 17 H. Yin, D. Han, W. Wang, Z. Hou, M. Zhou, Y. Han, I. Çaha, J. Cunha, M. Karimi, Z. Tai and X. Cao, *Chin. Chem. Lett.*, 2024, 110537.
- 18 G. Li, Z. Wang, Z. Li, Y. Long, C. Li, L. Chen, W. Wang, H. Yin, B. Zhang and Z. Hou, *Nano Mater. Sci.*, 2025, **2**, DOI: [10.1016/j.nanoms.2025.02.006](https://doi.org/10.1016/j.nanoms.2025.02.006).
- 19 W. Wang, M. Liu, Q. Wang, H. Tang, A. Li, W. Xu, Y. Zhu, Z. Hou, H. Zhang, Z. Tai and H. Yin, *Appl. Surf. Sci.*, 2025, **690**, 162613.
- 20 M. Imtiaz, Z. Chen, C. Zhu, H. Pan, I. Zada, Y. Li, S. W. Bokhari, R. Luan, S. Nigar and S. Zhu, *Electrochim. Acta*, 2018, **283**, 401–409.
- 21 C. Wang, X. Yang, M. Zheng and Y. Xu, *J. Alloys Compd.*, 2019, **794**, 569–575.
- 22 E. V. Beletskii, M. A. Kamenskii, E. V. Alekseeva, A. I. Volkov, D. A. Lukyanov, D. V. Anishchenko, A. O. Radomtseu, A. A. Reveguk, O. V. Glumov and O. V. Levin, *Appl. Surf. Sci.*, 2022, **597**, 153698.
- 23 X. Meng, Y. Xu, X. Sun, L. Xiong and Q. Wang, *J. Power Sources*, 2016, **326**, 389–396.
- 24 S. Xu, J. Zhou, J. Wang, S. Pathiranage, N. Oncel, P. Robert Ilango, X. Zhang, M. Mann and X. Hou, *Adv. Funct. Mater.*, 2021, **31**, 2101645.
- 25 H. Zhao, Z. Song, H. Gao, B. Li, T. Hu, F. Liu and H. Y. Sohn, *RSC Adv.*, 2020, **10**, 41403–41409.
- 26 M. Adhikari, E. Echeverria, G. Risica, D. N. McIlroy, M. Nippe and Y. Vasquez, *ACS Omega*, 2020, **5**, 22440–22448.
- 27 Q. T. Ain, S. H. Haq, A. Alshammari, M. A. Al-Mutlaq and M. N. Anjum, *Beilstein J. Nanotechnol.*, 2019, **10**, 901–911.
- 28 Y. Zhai, L. Xu and Y. Qian, *J. Power Sources*, 2016, **327**, 423–431.
- 29 J. Kang, K. Y. Yoon, J. E. Lee, J. Park, S. Chaule and J. H. Jang, *Nano Energy*, 2023, **107**, 108090.
- 30 P. Anushkaran, W. S. Chae, J. Ryu, S. H. Choi and J. S. Jang, *J. Mater. Chem. A*, 2024, **12**, 4702–4711.
- 31 N. D. Quang, P. C. Van, S. Majumder, J. R. Jeong, D. Kim and C. Kim, *J. Colloid Interface Sci.*, 2022, **616**, 749–758.
- 32 Y. Teng, X. D. Wang, J. F. Liao, W. G. Li, H. Y. Chen, Y. J. Dong and D. B. Kuang, *Adv. Funct. Mater.*, 2018, **28**, 1802463.
- 33 Y. Li, Y. Cheng, L. L. Daemen, G. M. Veith, A. M. Levine, R. J. Lee, S. M. Mahurin, S. Dai, A. K. Naskar and M. P. Paranthaman, *Phy. Chem. Chem. Phys.*, 2017, **19**, 22256–22262.
- 34 J. Wu, J. Zhao, B. Vaidhyanathan, H. Zhang, A. Anshuman, A. Nare and S. Saremi-Yarahmadi, *Materialia*, 2020, **13**, 100833.
- 35 V. R. Moreira, Y. A. R. Lebron, M. M. da Silva, L. V. de Souza Santos, R. S. Jacob, C. K. B. de Vasconcelos and M. M. Viana, *Environ. Sci. Pollut. Res.*, 2020, **27**, 34513–34528.
- 36 S. Kang, G. Wang, M. Fang, H. Wang, X. Wang and W. Cai, *J. Mater. Res.*, 2015, **30**, 1629–1638.
- 37 D. Vernekar and D. Jagadeesan, *Catal. Sci. Technol.*, 2015, **5**, 4029–4038.
- 38 S. Vishwanathan, S. Moolayadukkam, V. K. Gangaiah and H. R. Matte, *ACS Appl. Energy Mater.*, 2023, **6**, 2022–2030.
- 39 A. H. Wazir and I. W. Kundi, *J. Chem. Soc. Pak.*, 2016, **38**, 11–16.
- 40 R. A. Rochman, S. Wahyuningsih, A. H. Ramelan and Q. A. Hanif, *IOP Conf. Ser.: Mater. Sci. Eng.*, 2019, **509**, 012119.
- 41 L. Yu, S. Xi, C. Wei, W. Zhang, Y. Du, Q. Yan and Z. Xu, *Adv. Energy Mater.*, 2015, **5**, 1401517.
- 42 C. Xue, Y. He, Y. Liu, P. Saha and Q. Cheng, *Ionics*, 2019, **25**, 3069–3077.

- 43 Y. Gao, X. Du, Z. Hou, X. Shen, Y. W. Mai, J. M. Tarascon and B. Zhang, *Joule*, 2021, **5**, 860–1872.
- 44 X. Ma, M. Chen, B. Chen, Z. Meng and Y. Wang, *ACS Sustain. Chem. Eng.*, 2019, **7**, 19732–19738.
- 45 H. Qi, J. Huang, L. Tang, M. Ma, W. Deng and C. Zhang, *J. Electroanal. Chem.*, 2021, **882**, 115005.
- 46 Y. Sun, X. Hu, W. Luo, H. Xu, C. Hu and Y. Huang, *ACS Appl. Mater. Interfaces*, 2013, **5**, 10145–10150.
- 47 R. Cong, J. Y. Choi, J. B. Song, M. Jo, H. Lee and C. S. Lee, *Sci. Rep.*, 2021, **11**, 1283.
- 48 J. Im, J. D. Kwon, D. H. Kim, S. Yoon and K. Y. Cho, *Small Methods*, 2022, **6**, 2101052.
- 49 S. Peng, L. Yu, M. Sun, G. Cheng, T. Lin, Y. Mo and Z. Li, *J. Power Sources*, 2015, **296**, 237–244.
- 50 E. Mokaripoor, I. Kazeminezhad and R. Daneshtalab, *Mater. Today Commun.*, 2024, **38**, 108209.
- 51 B. Xiao, J. Liu, Q. Sun, B. Wang, M. N. Banis, D. Zhao, Z. Wang, R. Li, X. Cui, T. K. Sham and X. Sun, *Adv. Sci.*, 2015, **2**, 1500022.
- 52 W. Yang, Z. Wang, L. Chen, Y. Chen, L. Zhang, Y. Lin, J. Li and Z. Huang, *RSC Adv.*, 2017, **7**, 33680–33687.
- 53 D. C. Bock, G. H. Waller, A. N. Mansour, A. C. Marschilok, K. J. Takeuchi and E. S. Takeuchi, *J. Phys. Chem. C*, 2018, **122**, 14257–14271.
- 54 W. Wang, M. Hu, Z. Qu, Y. Dai, K. Chen and S. Lyu, *J. Energy Storage*, 2023, **74**, 109354.
- 55 J. Gong, X. Zeng, X. Zhou, R. Shi and K. Xia, *J. Electroanal. Chem.*, 2024, **952**, 117932.
- 56 Z. Zhang, H. Ying, P. Huang, S. Zhang, Z. Zhang, T. Yang and W. Q. Han, *Chem. Eng. J.*, 2023, **451**, 138785.